



Effects of tantalum addition on microstructure and properties of titanium alloy fabricated by laser powder bed fusion

ZHOU Li-bo(周立波)¹, SHU Jing-guo(舒京国)¹, SUN Jin-shan(孙金山)¹, CHEN Jian(陈荐)¹, HE Jian-jun(何建军)¹, LI Wei(李微)¹, HUANG Wei-ying(黄伟颖)¹, NIU Yan(牛焱)¹, YUAN Tie-chui(袁铁锤)²

1. Institute of Energy and Powder Engineering, Changsha University of Science and Technology,
Changsha 410114, China;

2. State Key Laboratory of Powder Metallurgy, Central South University, Changsha 410083, China

© Central South University Press and Springer-Verlag GmbH Germany, part of Springer Nature 2021

Abstract: The expanding of material library of laser powder bed fusion (L-PBF) is of great significance to the development of material science. In this study, the biomedical Ti-13Nb-13Zr powder was mixed with the tantalum particles (2 wt%–8 wt%) and fabricated by L-PBF. The microstructure consists of a β matrix with partially unmelted pure tantalum distributed along the boundaries of molten pool owing to the Marangoni convention. Because the melting process of Ta absorbs lots of energy, the size of molten pool becomes smaller with the increase of Ta content. The fine microstructure exists in the center of melt pool while coarse microstructure is on the boundaries of melt pool because of the existence of heat-affected zone. The columnar-to-equiaxed transitions (CETs) happen in the zones near the unmelted Ta, and the low lattice mismatch induced by solid Ta phase is responsible for this phenomenon. The recrystallization texture is strengthened while the fiber texture is weakened when the tantalum content is increased. Due to the formation of refined martensite α' grains during L-PBF, the compressive strengths of L-PBF-processed samples are higher than those fabricated by traditional processing technologies. The present research will provide an important reference for biomedical alloy design via L-PBF process in the future.

Key words: laser powder bed fusion; titanium alloys; tantalum; solidification microstructure; texture evolution

Cite this article as: ZHOU Li-bo, SHU Jing-guo, SUN Jin-shan, CHEN Jian, HE Jian-jun, LI Wei, HUANG Wei-ying, NIU Yan, YUAN Tie-chui. Effects of tantalum addition on microstructure and properties of titanium alloy fabricated by laser powder bed fusion [J]. Journal of Central South University, 2021, 28(4): 1111–1128. DOI: <https://doi.org/10.1007/s11771-021-4684-z>.

1 Introduction

Laser powder bed fusion (L-PBF) (commonly termed 3D printing) is resulting in a paradigm change across multiple industries, especially in the biomedical field [1–4]. Fabricating the net-shape metallic parts with complex geometries which are not achievable with conventional processing

technologies is one of the key advantages of L-PBF [5–8]. In addition, layer by layer SLM process provides product customization and short time to market, which are critical for the medical field since they can increase the success rate of the operation and shorten the operation time. For titanium-base parts, not just in biomedicine, SLM printed part can save 50% of the cost by basically missing out material loss and exorbitant machining casts [9].

Foundation item: Projects(51975061, 51775055) supported by the National Natural Science Foundation of China; Project(2020JJ5599) supported by the Natural Science Foundation of Hunan Province, China; Projects(19C0032, 19B033) supported by the Research Foundation of Education Bureau of Hunan Province, China

Received date: 2020-12-10; **Accepted date:** 2021-03-30

Corresponding author: ZHOU Li-bo, PhD, Lecture; E-mail: libozhou@csust.edu.cn; Tel: +86-731-85258409; ORCID: <https://orcid.org/0000-0001-6099-2062>

Using the SLM process, the buy-to-fly ratio (the weight of the raw material to that of the finished product) can close 1:1, which is unimaginable in the fields of traditional process [10, 11].

Even though the laser powder bed fusion (L-PBF) has many advantages, one of the drawbacks is the limitation of material library which seriously restricts the development of this technology [12–14]. Fortunately, the capability of L-PBF to process mixed powder has provided new and effective material research opportunities. Many researchers have done a lot of works in expanding the material library. SING et al [15] studied the titanium alloy with 50 wt% tantalum fabricated by L-PBF and the results show that Ti-Ta alloy can be a potential material for biomedical applications owing to its high strength to modulus ratio. VRANCKEN et al [16] researched the microstructure and mechanical properties of Ti-6Al-4V-ELI powder mixed with 10 wt% Mo powder and the novel microstructures consist of a β titanium matrix with randomly dispersed pure Mo particles. BARRIOBERO-VILA et al [17] revealed a new solidification and cooling path for α formation through L-PBF-printed Ti-La alloys. AZIZI et al [18] investigated the L-PBF-printed Ti-Al-Fe alloy and the results showed that globularization and formation of small β grains along the building direction occurred because of the presence of Fe. All of these titanium alloys are going to be used or have been applied in biomedical fields. However, safety concerns are raised on these alloys as they contain Fe or Al which can cause some side effects on the body [19, 20]. Therefore, the new titanium alloys that do not contain any of these toxic elements should be developed.

Since the high biocompatibility and corrosion resistance, tantalum (Ta) can be act as an excellent potential material for alloying with titanium alloys for biomedical [21]. What's more, Ta is a β stabilizer for titanium alloy. As we all know, β titanium alloy displays low modulus compared to the commonly used alloys which can reduce the adverse effect of stress shielding [22, 23]. Despite all its advantages, there is few research on Ta to modify the properties of titanium alloy, the superior high melt point (2996 °C) and the high density (16.6 g/cm³) of Ta will be responsible for this. Thanks for the development of industry, L-PBF, as a new advanced manufacturing technology, can solve this problem very well. During the L-PBF process, the

temperature higher than 3000 °C can be achieved at center of the molten pool [24–26], which is over the melt point of Ta and Ti metals. Our previous studies have also shown that the L-PBF can successfully fabricate pure Ta with high relative density. Therefore, in this paper, the mixtures of tantalum and titanium alloy powder (Ti-13Nb-13Zr alloy, a promising biomedical material, which has been researched in our previous studies [27, 28]) were fabricated by L-PBF. The phase transition and microstructure evolution, especially grain morphology and texture will be discussed. The mechanical properties of L-PBF-printed samples will also be evaluated. The results obtained in this paper will open up windows for target oriented biomedical alloy design in the future.

2 Experimental

2.1 Materials and L-PBF process

The Ti-13Nb-13Zr (wt%) powder with an average size of 31.3 μm obtained by gas atomized was used as a base material for the L-PBF process. As shown in Figure 1(a), most of the Ti-13Nb-13Zr particles present a spherical morphology with a smooth surface. The Ta particles, obtained by hydrogenation-dehydrogenation process, exhibit irregular shape and a small size compared to Ti-13Nb-13Zr powder, as observed in Figure 1(b). Four different Ti-13Nb-13Zr/Ta composites containing 2 wt%, 4 wt%, 6 wt% and 8 wt% Ta were prepared by ball milling with a planetary ball mill machine. For the sake of ease, the corresponding L-PBF-printed samples are denoted by 2Ta, 4Ta, 6Ta and 8Ta, respectively. In order to prevent the powder fluidity from being damaged, a series of ball mill exploration techniques have been carried out in our team, and the mill process was set as: ball-to-powder weight ratio (2:1), rotation speed (150 r/min) and mill time 3 h. Then the composites powders were dried in the vacuum at 323 K for 24 h and sieved (53 μm) to reduce the aggregated particles. Figure 1(c) shows the powder morphology of Ti-13Nb-13Zr/Ta with 2 wt% Ta content, apparently; the Ti-13Nb-13Zr/Ta composite also shows a spherical morphology and the Ta particles are randomly distributed.

All samples with dimensions of 10 mm×10 mm×10 mm were fabricated by L-PBF apparatus

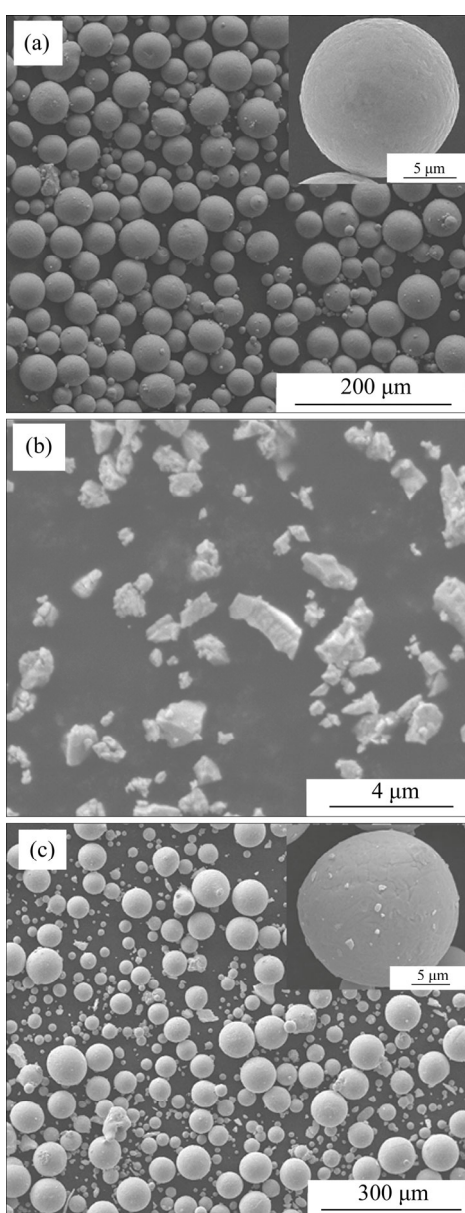


Figure 1 SEM images of gas atomized Ti-13Nb-13Zr (a), purity Ta particle (b) and Ti-13Nb-13Zr/Ta composite with 2 wt% Ta content (c)

(FS271M Farsoon, Inc., China), under a high-purity Ar atmosphere. The optimized process parameters were obtained in our other paper [23] and set as follows: the laser power (p) 325 W, laser speed (v) 1000 mm/s, layer thickness (d) 30 mm, hatch distance (h) 0.13 mm. The scanning strategy was set as each layer alternated by 67° and scanned using a continuous laser mode according to zigzag pattern, which can be found in our other papers [21, 28, 29]. The relative densities of 2Ta, 4Ta, 6Ta and 8Ta were calculated based on the Archimedes method and the results turned out to be 93.10%, 90.50%, 88.07% and 86.95%, respectively.

2.2 Characterization of microstructure and mechanical properties

The phase formation of the samples fabricated by L-PBF was characterized using X-ray diffraction (XRD, Rigaku D/MAX-2250). All tests were carried out on the longitudinal direction, owing to the anisotropy of SLM forming samples. The metallographic samples were prepared through the standard procedures and etched with Kroll's reagent. The optical microscope (OM), FEI Quanta FEG 250 field emission gun scanning electron microscope (FEG-SEM), electron backscattered diffraction (EBSD, EDAX TSL) and JEOL 2100F transmission electron microscope (TEM) were used to characterize the microstructures of samples. The mixture of 6% perchloric acid, 34% normal butanol and 60% methanol was used to prepare the samples for TEM and EBSD observation with electrolytic polishing at 243 K and 23 V. The element distribution was quantitatively analyzed by the electro-probe microanalyzer (EPMA JXA-8530F). Compressive test was performed using an Instron test 3369 machine, at a crosshead speed of 1 mm/min at room temperature. In order to ensure the uniformity of sample testing, all tests including optical, SEM, TEM and EPMA are carried out in the middle part of sample.

3 Results and discussion

3.1 Phase analysis

The XRD analysis of Ti-13Nb-13Zr/8Ta mixed powder and L-PBF-printed samples with different Ta additions has been conducted and the obtained patterns are shown in Figure 2(a). The XRD profiles do not show any secondary peak of Ta_2O_5 or other oxide, indicating that the mechanical properties of samples fabricated by L-PBF are not affected by any oxidation. As revealed in the XRD spectra, both the body-centered cubic (BCC) and hexagonal close-packed (HCP) phases can be detected in all samples. After L-PBF process, the α' phases become weaker while the β phases became stronger when compared to the initial powder. The repetitive melting and re-solidification in the L-PBF process leading to the decomposition of the α' martensite into β state partly can be used to explain this phenomenon [17]. No formation of new phase or decomposition of original phase occurred with various Ta contents during the

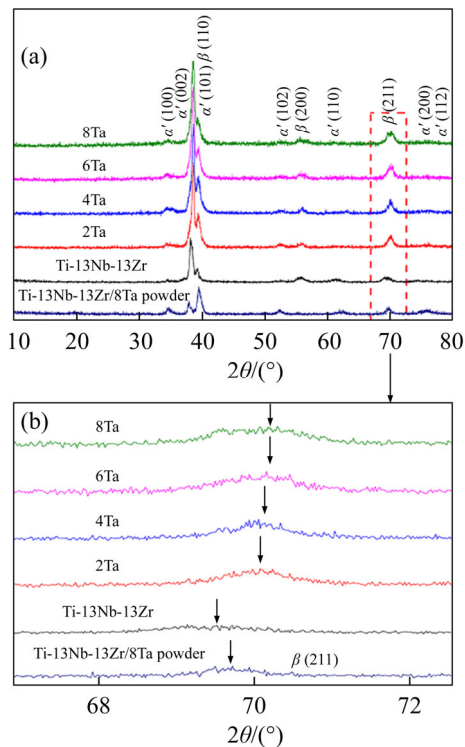


Figure 2 (a) XRD patterns of Ti-13Nb-13Zr/8Ta powder and L-PBF-printed samples Ti-13Nb-13Zr, 2Ta, 4Ta, 6Ta and 8Ta, and details

L-PBF process. It is easy to find that the β phase peaks are shifted to higher 2θ value with the increase of the Ta content, as shown in Figure 2(b). According to Bragg's law [30]:

$$2d \sin \theta = n\lambda$$

The increase of the 2θ value implies a decrease of the lattice plane distance d , which is believed to be caused by the formation of titanium-tantalum solid solution [31]. As the Ta content increases, the solubilization of Ta will be enhanced. The microscopy volume expansion usually occurs in the solid solution, which induces the stress that acts on the grain boundaries and may influence the lattice parameters [32]. In addition, the residual stress which enhances with the increase of Ta content also influences the lattice parameters at the grain boundaries [33]. Taking the results of MARI et al [34] into consideration, the lattice parameters are affected by the thermal strain, mechanical strain and lattice strain, in which the mechanical strain is caused by the residual stress and the lattice strain is caused by the solutes. What's more, with the increase of the residual stress, the solubilization of Ta will also be enhanced. When the Ta content increases to 8 wt%, the diffraction peak of β (200), as shown in

Figure 2(b), becomes significantly broadened and the intensity presents a considerable decrease, which implies that the crystals are refined and the fine microstructure is formed in this instant. The solidification cellular structures of 2Ta, 4Ta, 6Ta and 8Ta samples are shown in Figures 3(a)–(d), respectively. The constitutional super-cooling theory are responsible for the occurrence of cellular structures because of the high-temperature gradient and cooling rate in L-PBF process. For quantitative characterization of the cellular structures, the area-method can be used [21]:

$$S = \frac{\sqrt{A/M}}{N}$$

where A is the area of the SEM image; M is the magnification; N is the number of the cells on the target zone (as shown in Figures 3(a')–(d'), respectively), which is calculated by the software “ImageJ”. The results turn out that the average grain sizes of 2Ta, 4Ta, 6Ta and 8Ta samples are 0.185, 0.134, 0.112 and 0.071 μm , respectively. The sample 8Ta has the smallest average grain size compared with 2Ta, 4Ta and 6Ta samples, which is consistent with the results of XRD patterns as discussed above.

In order to further confirm the phase composition, the TEM analysis of 2Ta, 4Ta, 6Ta and 8Ta samples was carried out and the images are presented in Figures 4(a), (b), (c) and (d), respectively. It is apparent that all L-PBF-printed samples present a duplex microstructure and the martensite phases are distributed within the β matrix. The bright-TEM images indicate that the β grains exhibit a lamellar morphology and the hcp phase is α' martensite because of the needle-like morphology and fine size, as marked by red arrows [9]. The high-resolution transmission electron microscopy (HRTEM) and the corresponding Fast Fourier Transform (FFT) image were also conducted on 2Ta and 8Ta samples to confirm whether orthorhombic α'' martensite existed. The results further confirmed that the martensitic structure is α' martensite.

3.2 Molten pool shape evolution

Figure 5(a) shows the optical microscopy of the 2Ta sample. The typical semi-elliptical scan tracks of melt pool arising from the heat can be observed in the etched surface [28, 35]. The energy density used in this study is sufficient to fully melt the Ti-13Nb-13Zr powder but some of larger tantalum particles

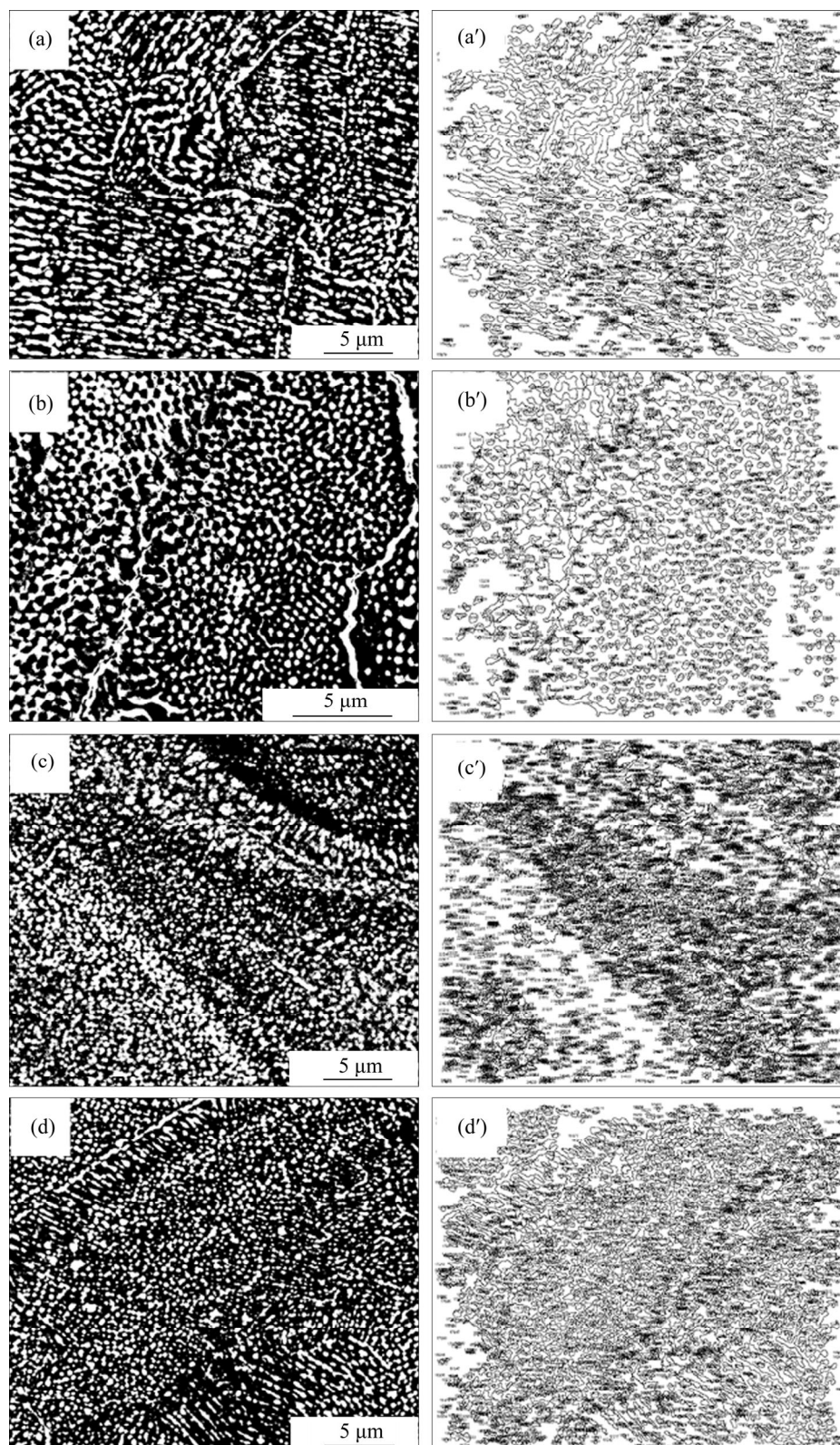


Figure 3 Representative SEM microstructure of 2Ta (a), 4Ta (b), 6Ta (c) and 8Ta (d) samples; ((a'), (b'), (c') and (d')) Number of statistical grains, respectively)

are only partially melted because of their high melting point. Therefore, many partially melted tantalum particles can be observed in the optical images, as marked by red arrows, especially in the

samples that contain high Ta content. The unmelted Ta particles confirmed by the EDX line scanning are mainly distributed at the boundaries of the molten pool owing to the Marangoni convention [36, 37].

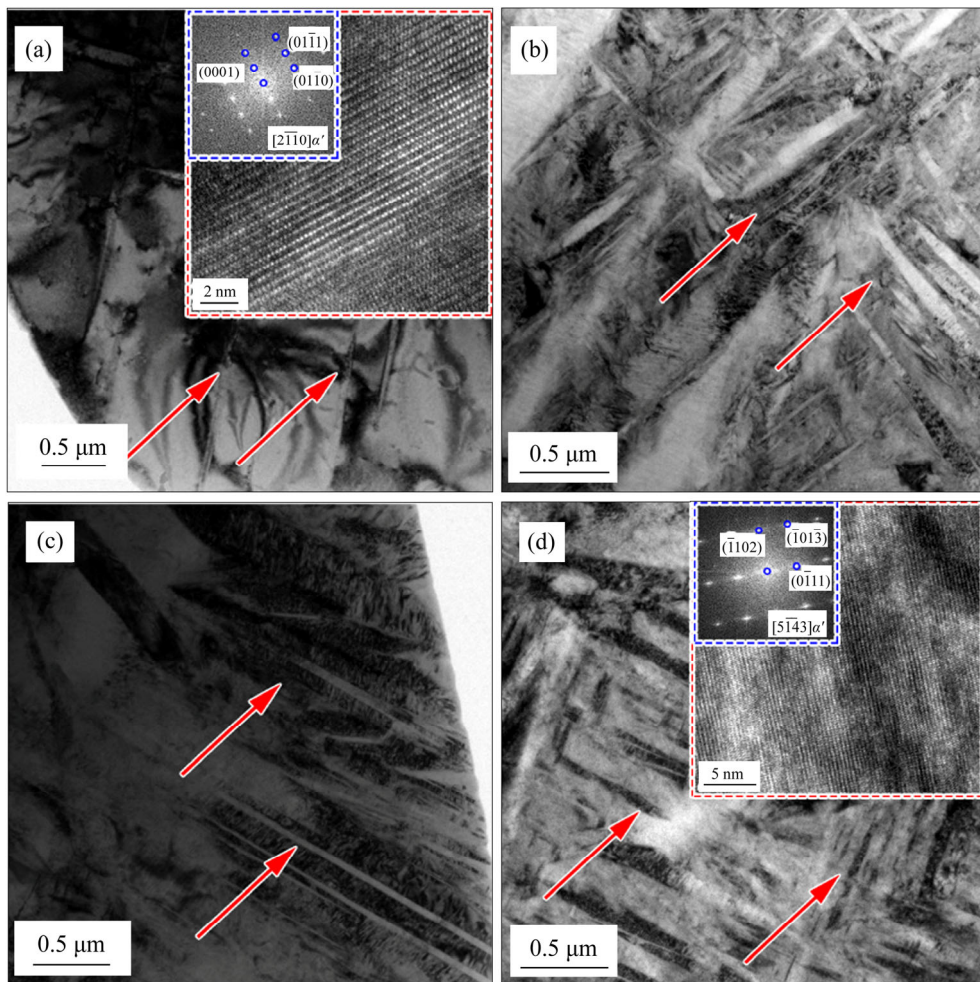


Figure 4 Bright-TEM images of L-PBF-printed samples 2Ta (a), 4Ta (b), 6Ta (c) and 8Ta (d) (the insets show high-resolution transmission electron microscopy (HRTEM) and the corresponding fast Fourier transform (FFT) image of α' martensite)

The convective streams within the melt pool are formed to rush the unmelted Ta particles to the boundaries of the melt pool and then solidify at the boundaries because of the high cooling rate during L-PBF process [38]. In order to identify elemental concentration, the EMPA mapping was conducted on the samples and the results are shown in Figure 6. The results indicate that the volume fraction of reinforcement Ta presents as 1.22 wt%, 2.95 wt%, 5.43 wt% and 6.54 wt%, respectively. From the obtained percentage of main elements, the areas of boundaries of melt pool rich in Ta while the area of central melt pool contains relatively slight amount of Ta, which further confirms the above view. With the increase of Ta content, the melt pool becomes more irregular, as marked by yellow circles, and the width and height of molten pools become smaller (Figures 5(b), (c) and (d)). The melting process of Ta will absorb lots of energy, which results in a lower

temperature in the molten pool, and thus a small size molten pool is formed. The presence of unmelted metal Ta in the molten pool will impede the movement of liquid fluid and increase the viscosity of melt pool, which result in the occurrence of some detrimental phenomena and finally lead to the reduction of density. Similar phenomena have been reported by GU et al [33] and ATTAR et al [39]. That can explain why the 8Ta sample has lower relative density compared with other samples.

In order to quantitatively analyze the influence of Ta addition on the size of melt pool, the plane perpendicular to the building direction was observed by SEM and the results are presented in Figure 7. Figures 7(a)–(d) show the microscopic characteristics of molten pool of the L-PBF-printed 2Ta, 4Ta, 6Ta and 8Ta samples, respectively. Compared with Figure 5, it is clearly shown that with the increase of Ta content, the width of melt

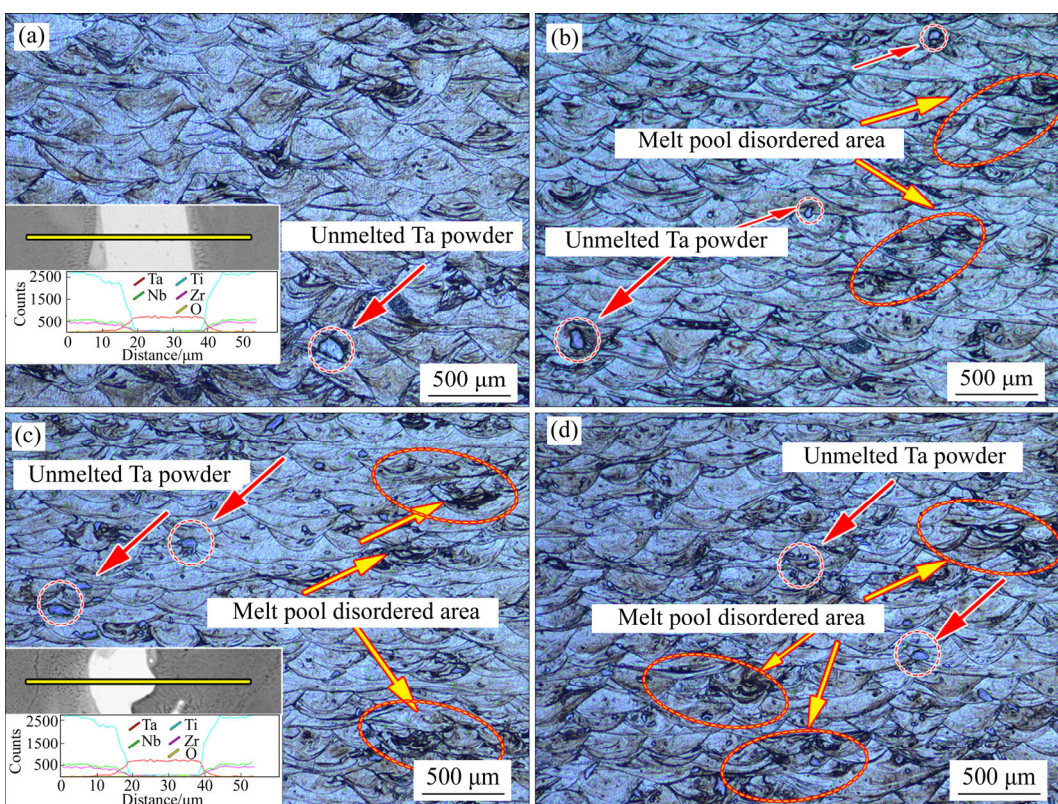


Figure 5 Microstructures of L-PBF-printed 2Ta (a), 4Ta (b), 6Ta (c) and 8Ta (d) samples (The EDX line scanning analysis results are described in insets)

pool declines. The average widths of melt pool were calculated using the software “ImageJ”. The results show that the width of melt pool is more than 150 μm in 2Ta sample (Figure 7(a)), while it is 50 μm in 8Ta sample (Figure 7(d)).

3.3 Microstructure and texture evolution

Figure 8(a) illustrates the SEM images of 2Ta sample along the building direction, in which the boundaries of melt pool are visible. Most grains grow epitaxially across the melt pool boundaries, which is a typical characteristic of the microstructure in L-PBF-printed parts. This can be attributed to the remelting of previous layers and the diffusion phenomenon during L-PBF process [40]. As seen in the picture, two main kinds of microstructures can be observed in the sample. The average width of grains is relatively small at the central of melt pool, while the microstructure contains coarser grains at the overlap zones of multiple melt pools and the edge zone of the melt pools, which is magnified in Figure 8(c). This can be explained by two reasons: according to earlier studies [41, 42], the liquid-solid interface velocities and the temperature gradient are relatively larger in the melt pool of L-PBF when

compared with traditional technologies, so the finer microstructure is formed at the center of melt pool. The heat-affected zone (HAZ) exists at the boundaries of melt pool and its high temperature will induce the grain growth [43]. Besides, the overlap zones of multiple melt pool may have been reheat-affected several times owing to the unique processing method of L-PBF [44], that is why the grains in overlap zones are coarser than that in the center of melt pool. There is no unmelted Ta in the melt pool zone, the fine grains present a directional growth along the z-axis since the direction of the temperature gradient is from the edge of the melt pool to its center, as presented in Figures 8(b) and (d).

Since the duration of laser irradiation that acts on the powder is extremely short, the instantaneous temperature is insufficient to melt the Ta powder completely, thus leading to a simultaneous presence of liquid phase and solid phase in melt pool. The solid Ta phase will act as heterogeneous nucleation sites because of the low lattice mismatch [5, 17]. Therefore, two typical microstructures can be observed, namely oriented cellular substructures near the Ta nucleation site and equiaxed

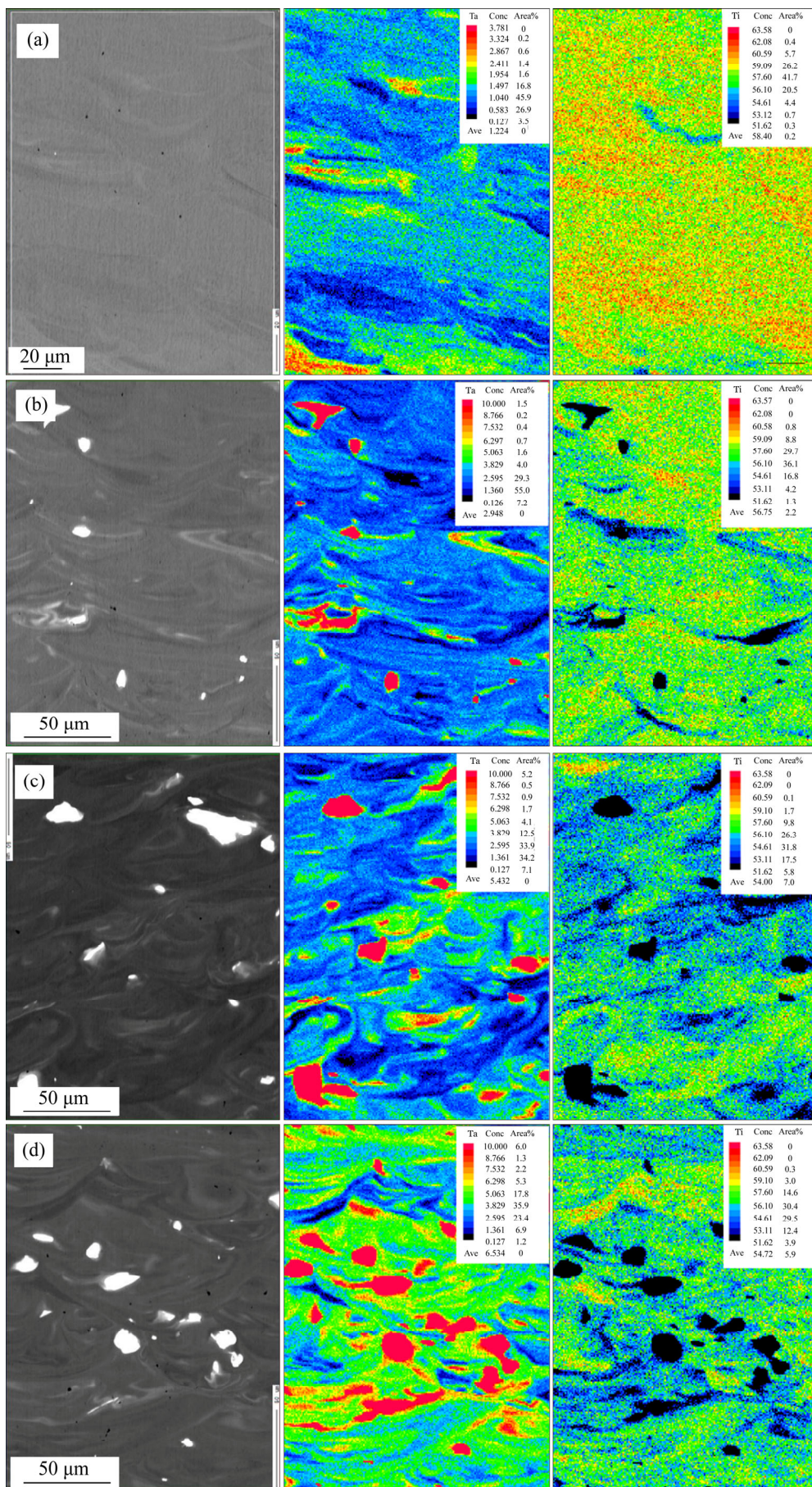


Figure 6 EMPA mapping results presenting distribution of element in base metal: (a) 2Ta; (b) 4Ta; (c) 6Ta; (d) 8Ta

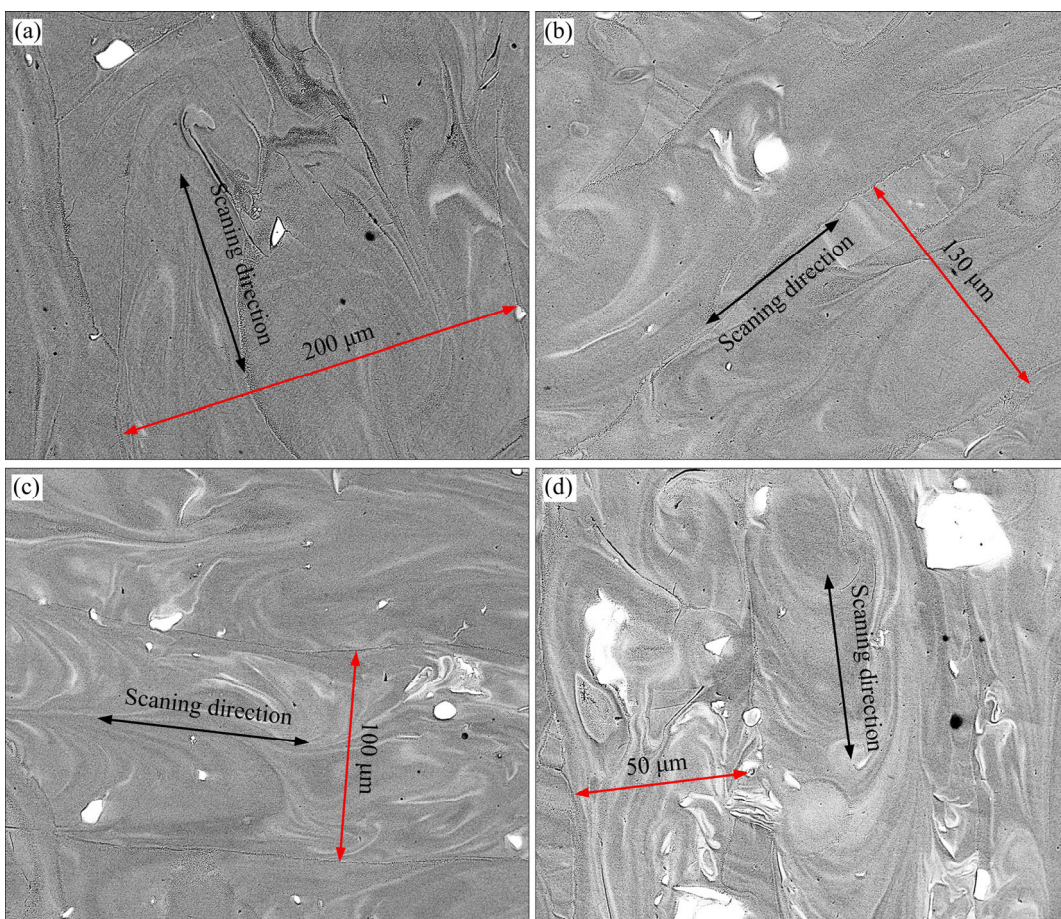


Figure 7 SEM images of L-PBF-printed samples: (a) 2Ta; (b) 4Ta; (c) 6Ta; (d) 8Ta

microstructures converted from the cellular substructures, as shown in Figure 9(a), which is consistent with the results of ZHANG et al [45]. In addition to the grain size, the grain morphology would also determine the mechanical properties of the parts. Taking the results of REN et al [46] and WANG et al [5] into consideration, the columnar-to-equiaxed transitions (CETs) of grains formation have been related to the temperature gradient G and growth rate R . As the G/R ratio continuously varies from low value to high value, equiaxed dendritic and cellular microstructure are successively expected [46], as shown in Figure 9(d). In addition, the complex heat transfer behavior in the zones near unmelted Ta results in the nearly isotropous distribution of temperature gradient, and thus facilitates the formation of cellular substructure in these regions [16]. Generally, due to the higher thermal diffusion rate in the region of solid phase, the melts in these regions tend to solidify preferentially along the edge of the pool while nucleating and growing in typical columnar dendrites [47]. The bright-TEM image (Figure 9(b))

shows that the orientation of cellular substructure is along $a(001)$. The high-magnificent TEM image (Figure 9(c)) shows that the length of the cellular grains is longer than 600 nm and the width of the cellular grains is 80 nm.

For the purpose to investigate the effect of Ta content on the texture evolution, the EBSD was conducted on the building direction of samples 2Ta and 4Ta. Figures 10(a) and (d) show the image quality of samples 2Ta and 4Ta, respectively. As shown in Figure 10(a), the bulk microstructure consisted of columnar prior β grains, which extend through many layers. The fine α' martensite can be observed within prior β grains. These microstructure features are not characteristics of typical transformation mechanisms, namely martensite $\beta \rightarrow \alpha'$ transformation which fills parent β grains with α' plates. Similar results have been reported in Ref. [17] where a 2 wt% La addition to pure Ti alloy leads to a similar microstructure. Different from the Figure 10(a), the columnar grains in sample 4Ta (Figure 10(d)) are not as clear as those in sample 2Ta, the increased Ta is primarily responsible for this

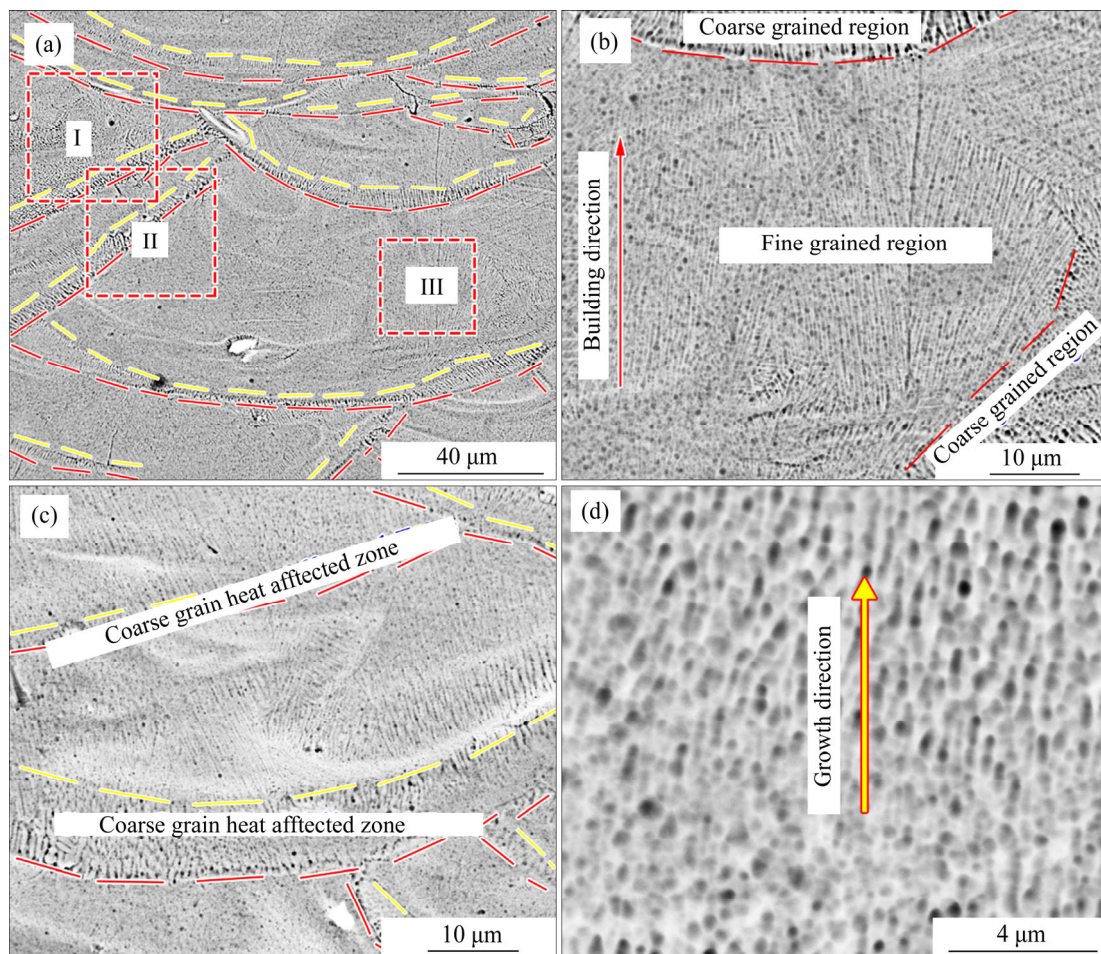


Figure 8 (a) SEM-BSE image of microstructure in the build direction of sample 2Ta (the red dotted line is the boundaries of melt pool and heat-affected zone is the intermediate region between the red dotted line and yellow dotted line); (b) SEM-BSE image of region I; (c) SEM-BSE image of region II; (d) SEM-BSE image of region III

phenomenon, which acts as a nucleation site [48]. The inverse pole figures (IPFs) of the samples 2Ta and 4Ta are shown in Figures 10(b) and (d), respectively. The β columnar grains grow epitaxially across the multiple melt pools along the z axis, which is consistent with the results in Figure 8. For sample 4Ta, the IPF shows that the microstructure consists mostly of equiaxed β grains and the superfine equiaxed α' martensite, as shown in Figures 10(e) and (f). For the hierarchical microstructure shown in Figure 10(e), the constitutional undercooling governed by liquid/solid interfacial instabilities [17, 49, 50] may be responsible for the grain nucleation, since it can provide the driving force. Phase analysis reveals that the contents of α' and β phases are calculated to be respectively 32.3% and 67.8% in sample 2Ta. The content of α' phase in sample 4Ta is reduced to 20.2% while the content of β phase is elevated to 79.8%. The increase of Ta content reduces the transition temperature of $\beta \rightarrow \alpha$ phase as

well as the formation interval of α phase, making the transition of $\beta \rightarrow \alpha$ more difficult. That is the one of the reasons why the α' phases decrease while the β phases increase with the increase of Ta content.

For further understanding the influence of Ta addition on the crystallographic texture of L-PBF-printed samples, the pole figures (PFs) and inverse pole figures (IPFs) showing β crystallographic texture of the samples 2Ta and 4Ta are obtained from the EBSD data (Figure 10), and the results are shown in Figures 11(a), (c) and (b), (d), respectively. Different from the L-PBF-printed Ti-13Nb-3Zr alloy [27], the two samples do not exhibit a $(110)_\beta$ fiber texture along the building direction. It can be easily found that the texture intensities of β phase decrease with the rise of the content of Ta, as shown in Figures 11(a) and (b), suggesting that the CET induces not only a morphological change in the microstructure, but a crystallographic texture variation as well [17]. To make a quantitative

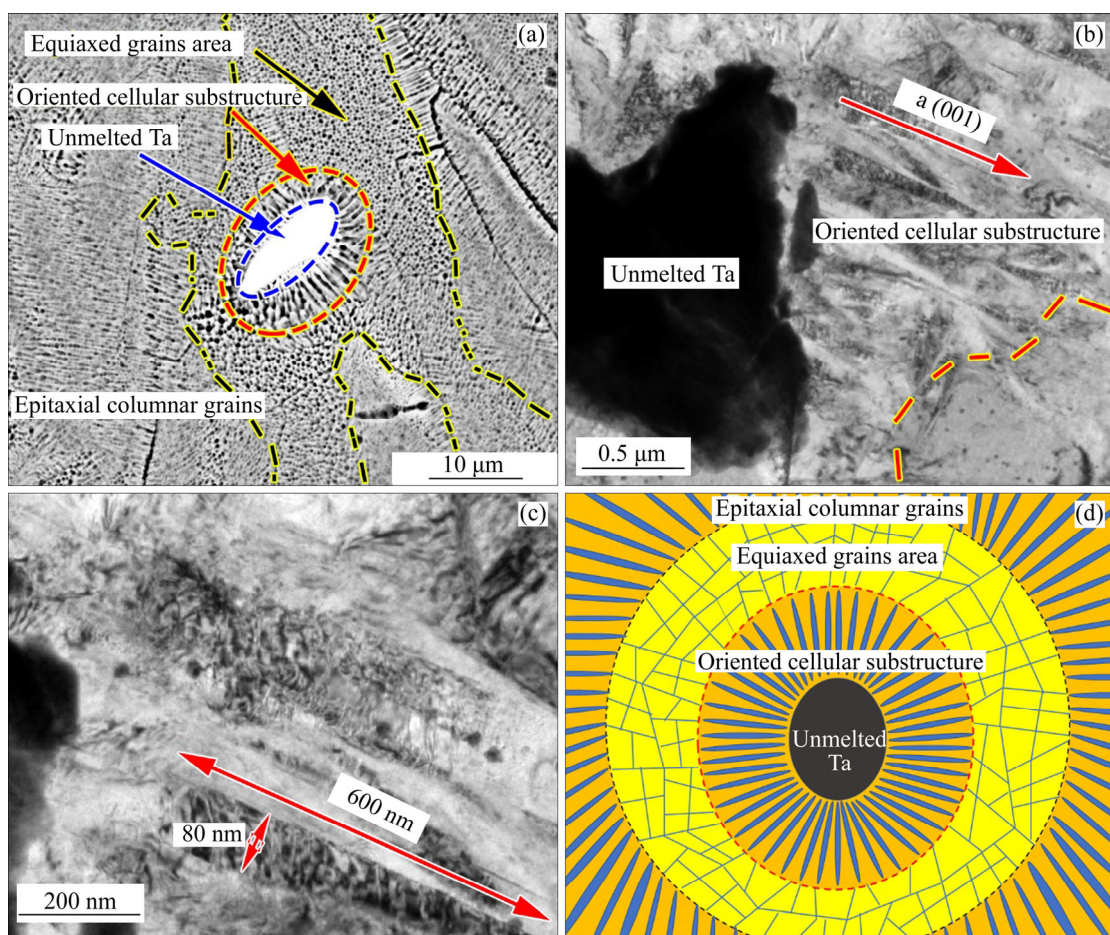


Figure 9 (a) SEM image of typical microstructures of L-PBF-printed 6Ta sample in scanning direction with unmelted Ta; (b) TEM image showing orientated cellular substructure; (c) High-magnificent TEM image and (d) schematic showing the microstructure evolution in the area of unmelted Ta

analysis on the texture intensities of samples 2Ta and 4Ta, the texture index is defined by Eq. (1) [24]:

$$\text{Texture Index} = \int_{\text{Eulerspace}} f(g)^2 dg \quad (1)$$

where f presents the orientation distribution; g presents the Eulerspace coordinates and $f(g)$ presents the ODF. The maximum texture indexes of samples 2Ta and 4Ta are calculated to be 16.522 and 6.334, respectively, based on Eq. (1). The value of texture index can be used to describe the texture strength, since both of them have the same unit and the texture strength is proportional to the texture indexes [27]. What's more, it is also implied that the fiber texture is weakened while the recrystallization texture is gradually strengthened with the increase in Ta content, as indicated in Figures 11(c) and (d).

The typical EBSD images of α' martensites in Figures 10(b) and (e) have been investigated to further determine the influence of Ta content on the texture evolution of α' phase. The shape of α' phase

is gradually changed from the needle-like to equiaxial with the increase of Ta content, as observed in Figures 12(a) and (d). Figures 12(b), (c) and (e), (f) show the detailed α' phase texture analysis on samples 2Ta and 4Ta, respectively. Obviously, the results indicate that the Ta content has a significant effect on the texture evolution. The $\{0001\}$ fiber texture can be observed in Figure 12(c) and the strength can be calculated to be 27.341 based on Eq. (1). With the increase of Ta content, the fiber texture is weakened while the recrystallization texture is gradually strengthened, as shown in Figure 12(f), which is in consistence with the formation of equiaxial grains in sample 4Ta. Similar results were obtained by LI et al [24] who studied the influence of TiB_2 content on the texture of L-PBF-printed TiAl/TiB_2 metal matrix composites.

3.4 Mechanical properties

In order to understand the influence of Ta

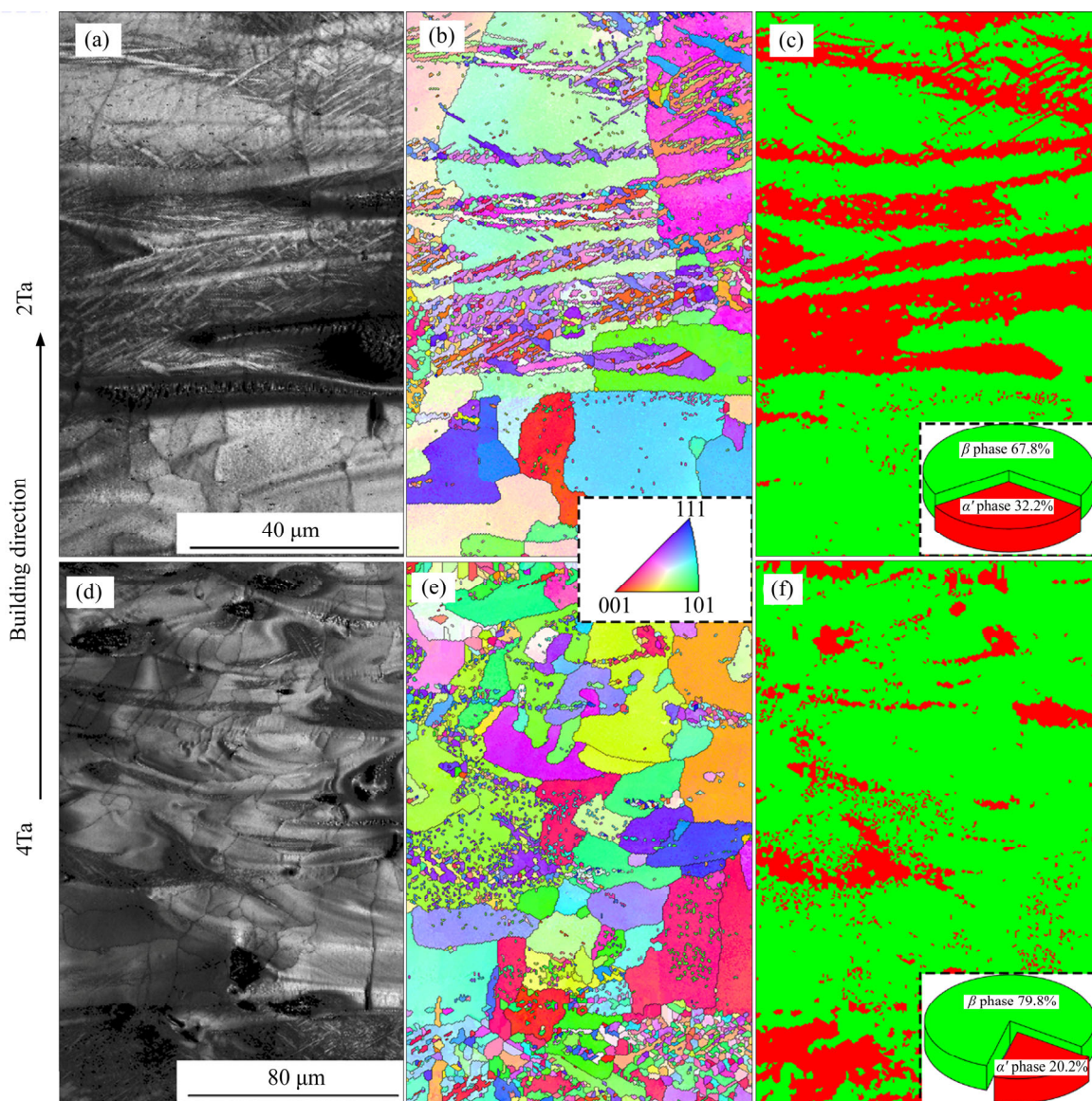


Figure 10 EBSD image of samples 2Ta (a) and 4Ta (d); Orientation maps of samples 2Ta (b) and 4Ta (e); Phase composition and distribution of samples 2Ta (c) and 4Ta (f)

content on the compression properties, room temperature compression tests were performed on the samples with various Ta content processed by L-PBF. The ultimate compressive strength, yield strength and ductility of the samples are depicted in Figure 13. The results show that the ultimate compressive strength and the yield strength of the 0Ta samples without Ta (1612.58 and 1212.92 MPa) are higher than 2Ta samples (1451.38 and 1125.76 MPa), 4Ta samples (1474.53 and 1045.9 MPa), 6Ta samples (1428.58 and 990.1 MPa) and 8Ta samples (1430.64 and 1019.68 MPa), while the ductility was opposite (10% in 0Ta samples to 11% in 2Ta samples, 16% in 4Ta samples, 17% in 6Ta samples and 19% in 8Ta samples). The higher relative density of 0Ta

samples (97.8%) is responsible for the higher compressive strength and yield strength compared to the other samples. The yield strength decreases with the increase of Ta content, since the relative density decreases with the increase of Ta content. The yield strength can be significantly affected by the size and location of pores [51]. What's more, the decrease of the content of α' martensitic structure also results in the decrease of yield strength, since the α' martensitic is a hard and brittle phase [29]. The results of Figure 11 show that the recrystallization texture is gradually strengthened while the {0001} fiber texture is weakened. The compressive strength is known to show a texture orientation dependence, even though the Ti alloy exhibits a high crystal symmetry [48].

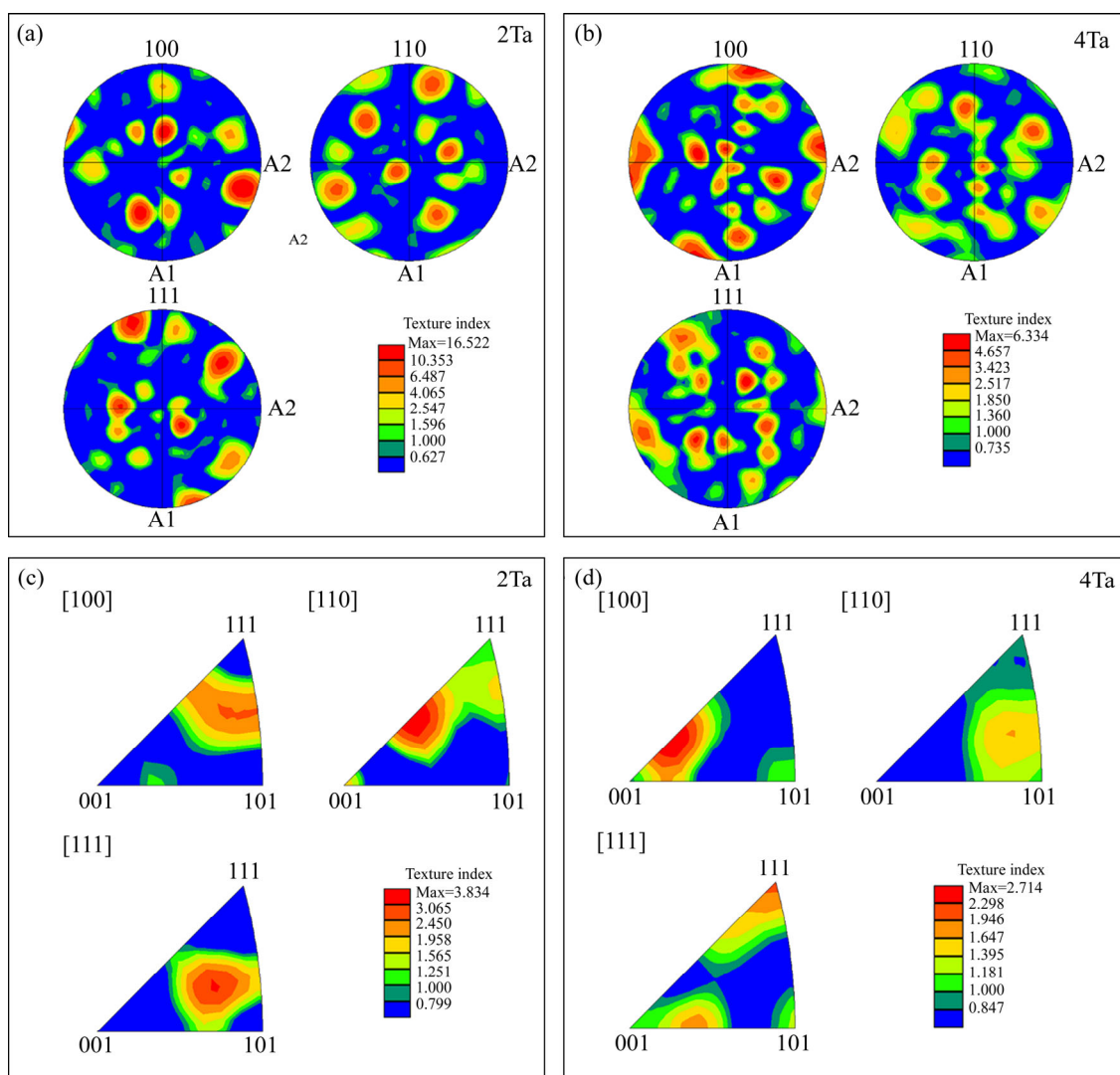


Figure 11 Pole figures and inverse pole figures showing (001), (110) and (111) crystallographic textures of L-PBF-printed samples: (a, c) Sample 2Ta; (b, d) Sample 4Ta

The {0001} fiber texture is weakened, while the recrystallization texture is gradually strengthened which tends to cause the basal slips, leading to the decrease of hardening rate, thus affecting the yield strength of the samples. It is worth noting that all of the L-PBF-fabricated samples showed much higher compressive strength and yield strength than the conventional produced samples [52] (Dynamic globularization: 1119 and 1010 MPa; solution treatment + aging: 716 and 619 MPa). The formation of martensite α' structure and the grain refinement because of the large cooling rate can be used to explain this enhancement of compressive strength and yield strength. The OM and SEM observations performed on the deformed samples were used to identify the fracture characteristics and mechanisms. An arc-shaped shear band can be observed from the

top view of the L-PBF-fabricated samples, as shown in Figure 13(b). Figure 13(c) demonstrates that the fracture in the specimens occurring along the plane inclined at an angle of 45° plane to the compression axis. The similar fracture mechanism has been reported by XIAO et al [53] about Ti-6Al-4V alloy.

In order to further understand the fracture mechanism, the typical fracture surfaces of samples 2Ta, 4Ta, 6Ta and 8Ta under quasi-static compression test are shown in Figures 14(a)–(d), respectively. The obvious parabolic dimples with elongation along the shear direction are observed in all of samples, indicating that the specimens undergo considerable plastic deformations. There were no significant unmelted areas observed in the fracture surfaces (Figures 14(a) and (b)), which means that samples 2Ta and 4Ta endured more homogenous

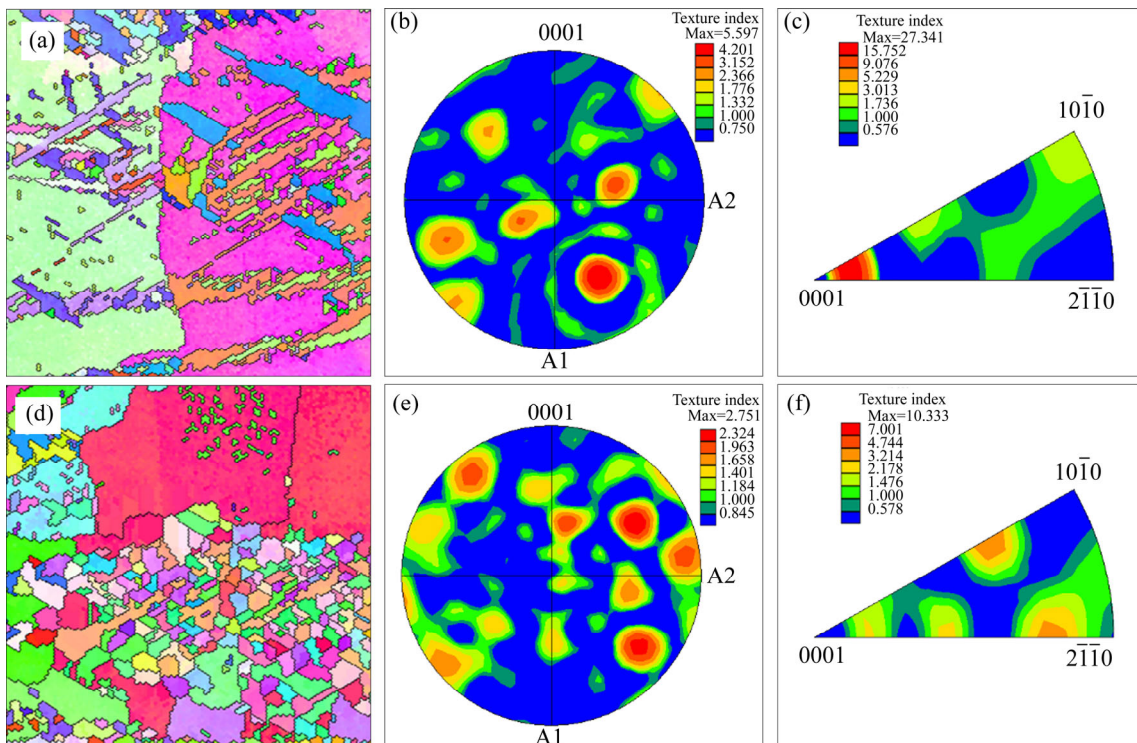


Figure 12 Detailed EBSD images of α' martensites showing the EBSD orientation maps of sample 2Ta (a) and sample 4Ta (d); Pole figures of 2Ta (b) and 4Ta (e); Inverse pole figures of 2Ta (c) and 4Ta (f)

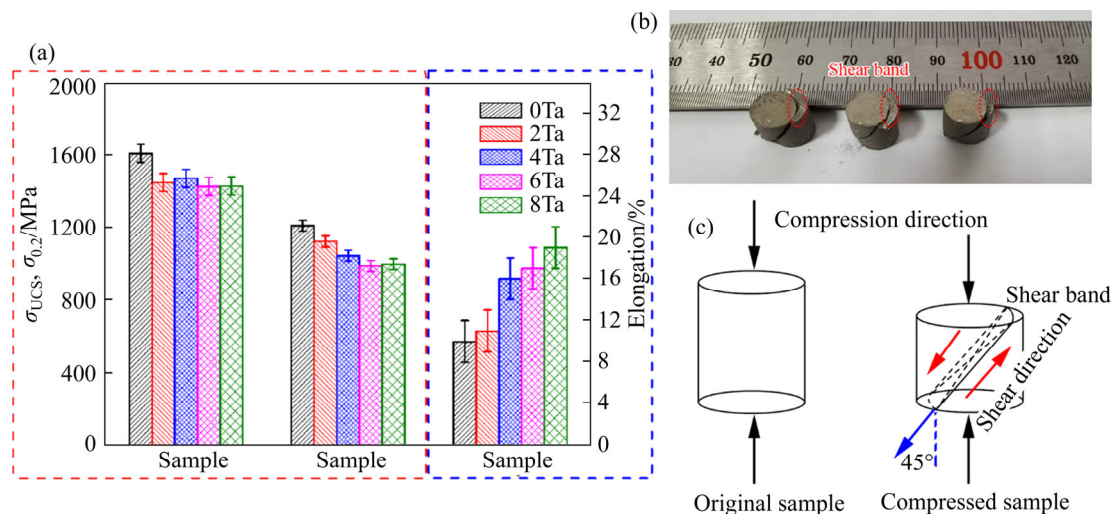


Figure 13 (a) Calculated ultimate compression strength, yield strength and ductility of the samples with various Ta content (Each value is determined from an average of 3 measurements; 0Ta represents Ti-13Nb-13Zr alloy; σ_{UCS} represents ultimate compression strength; $\sigma_{0.2}$ represents yield strength; (b) Side view of deformed samples; (c) Schematic of fracture characteristics and orientation of shear band of L-PBF-fabricated samples under compression

compressive deformation. The 8Ta sample has the highest elongation, contributed to the fact that the unmelted areas and porosities can absorb more compressive deformation than grains because of the stress localization on the defects as shown in Figure 14(d), which is consistent with the results of ATTAR et al [54]. Due to the varying size, irregular shape and random distribution of defects, the stress

and strain through the whole sample are not uniform, which results in the grain deformation not significant. This is responsible for the fact that the 8Ta sample has the minimum grain size while has no significant increase of the yield strength. Meanwhile, porosities appear ellipsoidal and walls of unmelted areas into contact can be observed in Figures 14(c) and (d), respectively.

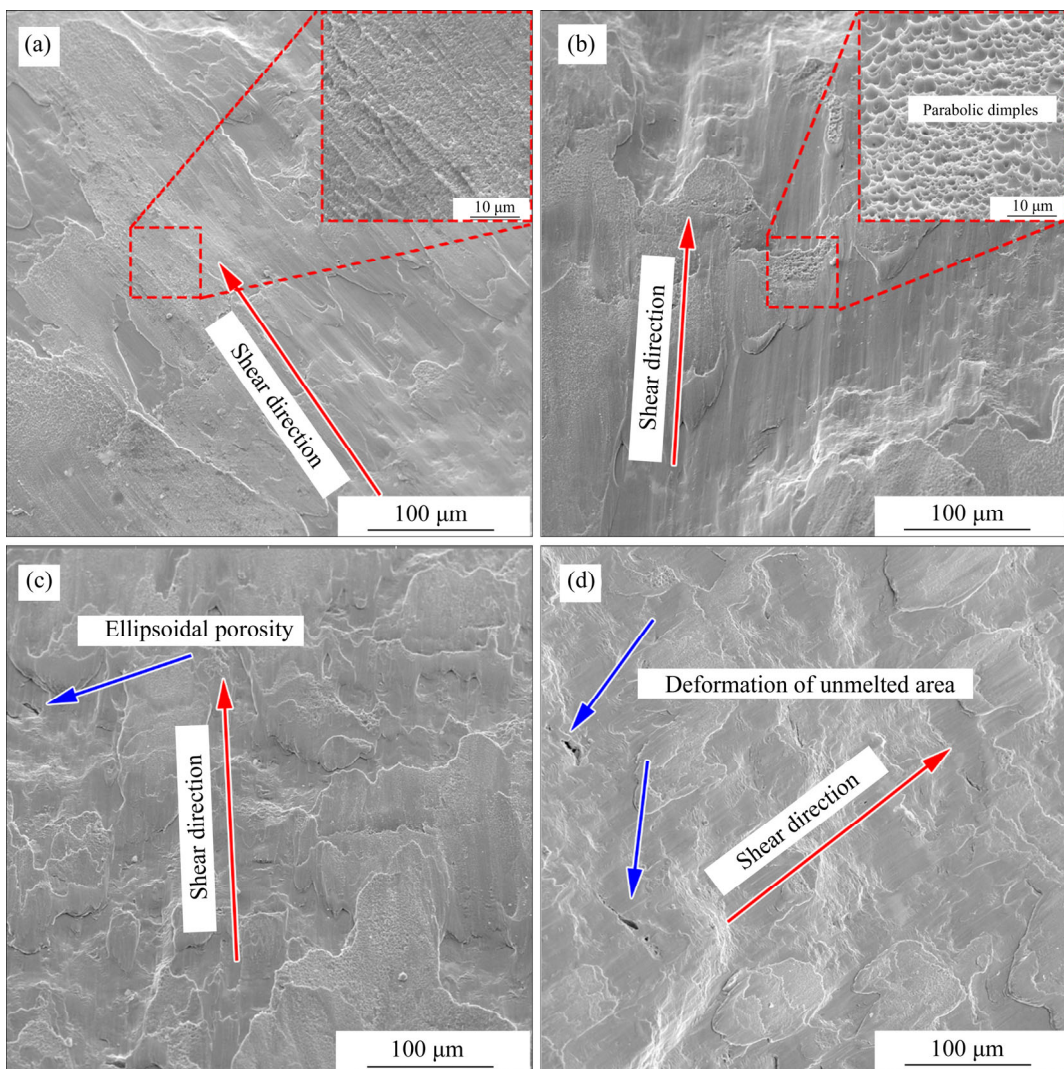


Figure 14 Typical fracture morphologies of L-PBF-fabricated parts: (a) 2Ta samples; (b) 4Ta samples; (c) 6Ta samples; (d) 8Ta samples

4 Conclusions

The phase transformation, melt pool evolution, texture evolution, microstructure features and nano-hardness of L-PBF-printed Ti-13Nb-13Zr/Ta alloys have been studied. The main conclusions are drawn as follows:

1) With the increase of Ta content, the width and height of the molten pools become smaller, and the unmelted Ta is distributed at the boundaries of melt pools. The width of the melt pool is more than 150 μm in 2Ta sample while 50 μm in 8Ta sample.

2) Two different microstructures exist in the L-PBF-fabricated Ti-13Nb-13Zr/Ta samples. The finer microstructure is formed at the center of melt pool, while the relatively coarser grains can be observed at the edge zones of melt pool and the overlap zones.

Near the unmelted Ta, there are also two typical microstructures, namely oriented cellular substructures near the Ta nucleation site and equiaxed grains converted from cellular substructures.

3) With the increase of Ta content, the content of α' phase decreases while the β phase increases and the columnar to equiaxed transition (CET) has been observed. The CET induces not only a morphological change in the microstructure, but a crystallographic texture variation. With the increase of Ta content, the recrystallization texture is strengthened while the fiber texture is gradually weakened.

4) The compressive strength of all samples increased noticeably compared to those of produced by conventional techniques due to the formation of martensite α' structure and grain refinement.

Contributors

ZHOU Li-bo contributed to the paper writing, designed the project, carried out data processing, and performed data analysis. SHU Jing-guo, SUN Jin-shan performed data analysis. CHEN Jian, HE Jian-jun, LI Wei, HUANG Wei-ying and NIU Yan offered some valuable suggestions for the contents of the manuscript. YUAN Tie-chui offered the specimen, performed data analysis. All authors replied to reviewers' comments and revised the final version.

Conflict of interest

ZOUE Li-bo, SHU Jing-guo, SUN Jin-shan, CHEN Jian, HE Jian-jun, LI Wei, HUANG Wei-ying, NIU Yan, YUAN Tie-chui declare that they have no conflict of interest.

References

- [1] LIU Y J, LI S J, WANG H L, HOU W T, HAO Y L, YANG R, SERCOMBE T B, ZHANG L C. Microstructure, defects and mechanical behavior of beta-type titanium porous structures manufactured by electron beam melting and selective laser melting [J]. *Acta Mater.*, 2016, 113: 56–67. DOI: <https://doi.org/10.1016/j.actamat.2016.04.029>.
- [2] ZHANG L C, KLEMM D, ECKERT J, HAO Y L, SERCOMBE T B. Manufacture by selective laser melting and mechanical behavior of a biomedical Ti-24Nb-4Zr-8Sn alloy [J]. *Scr Mater.*, 2011, 65: 21–24. DOI: <https://doi.org/10.1016/j.scriptamat.2011.03.024>.
- [3] SING S L, YEONG W Y. Laser powder bed fusion for metal additive manufacturing: Perspectives on recent developments [J]. *Virtual Phys Prototyp.*, 2020, 15: 359–370. DOI: <https://doi.org/10.1080/17452759.2020.1779999>.
- [4] HUANG S, SING S L, de LOOZE G, WILSON R, YEONG W Y. Laser powder bed fusion of titanium-tantalum alloys: Compositions and designs for biomedical applications [J]. *J. Mech Behav Biomed Mater.*, 2020, 108: 103775. DOI: <https://doi.org/10.1016/j.jmbbm.2020.103775>.
- [5] WANG P, DENG L, PRASHANRTH K G, PAULY S, ECKERT J, SCUDINO S. Microstructure and mechanical properties of Al-Cu alloys fabricated by selective laser melting of powder mixtures [J]. *J Alloys Compd.*, 2018, 735: 2263–2266. DOI: <https://doi.org/10.1016/j.jallcom.2017.10.168>.
- [6] WANG P, ECKERT J, PRASHANRTH K G, WU M W, KABAN I, XI L X, SCUDINO S. A review of particulate-reinforced aluminum matrix composites fabricated by selective laser melting [J]. *Trans Nonferrous Met Soc China*, 2020, 30: 2001–2034. DOI: [10.1016/S1003-6326\(20\)65357-2](https://doi.org/10.1016/S1003-6326(20)65357-2).
- [7] BI J, LEI Z L, CHEN Y B, CHEN X, TIAN Z, LU N N, QIN X K, LIANG J W. Microstructure, tensile properties and thermal stability of AlMgSiScZr alloy printed by laser powder bed fusion [J]. *J Mater Sci Tech*, 2021, 69: 200–211. DOI: <https://doi.org/10.1016/j.jmst.2020.08.033>.
- [8] BI J, LEI Z L, CHEN Y B, CHEN X, LU N N, TIAN Z, QIN X K. An additively manufactured Al-14.1Mg-0.47Si-0.31Sc-0.17Zr alloy with high specific strength, good thermal stability and excellent corrosion resistance [J]. *J Mater Sci Tech*, 2021, 67: 23–35. DOI: <https://doi.org/10.1016/j.jmst.2020.06.036>.
- [9] ZHOU L, YUAN T, LI R, TANG J, WANG M, MEI F. Microstructure and mechanical properties of selective laser melted biomaterial Ti-13Nb-13Zr compared to hot-forging [J]. *Mater Sci Eng A*, 2018, 725: 329–340. DOI: <https://doi.org/10.1016/j.msea.2018.04.001>.
- [10] QIN Y, QI Q, SHI P, SCOTT P J, JIANG X. Automatic generation of alternative build orientations for laser powder bed fusion based on facet clustering [J]. *Virtual Phys Prototyp.*, 2020, 15: 307–324. DOI: <https://doi.org/10.1080/17452759.2020.1756086>.
- [11] SING S L, HUANG S, YEONG W Y. Effect of solution heat treatment on microstructure and mechanical properties of laser powder bed fusion produced cobalt-28chromium-6molybdenum [J]. *Mater Sci Eng A*, 2020, 769: 138511. DOI: <https://doi.org/10.1016/j.msea.2019.138511>.
- [12] GU D, WANG H, DAI D, YUAN P. Rapid fabrication of Al-based bulk-form nanocomposites with novel reinforcement and enhanced performance by selective laser melting [J]. *Scr Mater.*, 2015, 96: 25–28. DOI: <https://doi.org/10.1016/j.scriptamat.2014.10.011>.
- [13] JIANG L Y, LIU T T, ZHANG C D, ZHANG K, LI M C, MA T, LIAO W H. Preparation and mechanical properties of CNTs-AlSi10Mg composite fabricated via selective laser melting [J]. *Mater Sci Eng A*, 2018, 734: 171–177. DOI: <https://doi.org/10.1016/j.msea.2018.07.092>.
- [14] VILARDELL A M, YADROITSEV I, YADROITSAVA I, ALBU M, TAKATA N, KOBASHI M, KRAKHMALEV P, KOUPRIANOFF D, KOTHLEITNER G, du PLESSIS A. Manufacturing and characterization of in-situ alloyed Ti6Al4V(ELI)-3 at.% Cu by laser powder bed fusion [J]. *Addit Manuf.*, 2020, 36: 101436. DOI: <https://doi.org/10.1016/j.addma.2020.101436>.
- [15] SING S L, YEONG W Y, WIRIA F E. Selective laser melting of titanium alloy with 50 wt% tantalum: Microstructure and mechanical properties [J]. *J Alloys Compd.*, 2016, 660: 461–470. DOI: <https://doi.org/10.1016/j.jallcom.2015.11.141>.
- [16] VRANCKEN B, THIJS L, KRUTH J P, van HUMBEECK J. Microstructure and mechanical properties of a novel β titanium metallic composite by selective laser melting [J]. *Acta Mater.*, 2014, 68: 150–158. DOI: <https://doi.org/10.1016/j.actamat.2014.01.018>.
- [17] BARRIOBERO-VILA P, GUSSONE J, STARK A, SCHELL N, HAUBRICH J, REQUENA G. Peritectic titanium alloys for 3D printing [J]. *Nat Commun.*, 2018, 9: 1–9. DOI: <https://doi.org/10.1038/s41467-018-05819-9>.
- [18] AZIZI H, ZUROB H, BOSE B, REZA GHIAASIAAN S, WANG X, COULSON S, DUZ V, PHILLION A B. Additive manufacturing of a novel Ti-Al-V-Fe alloy using selective laser melting [J]. *Addit Manuf.*, 2018, 21: 529–535. DOI: <https://doi.org/10.1016/j.addma.2018.04.006>.
- [19] LIU Y J, LI S J, ZHANG L C, HAO Y L, SERCOMBE T B. Early plastic deformation behaviour and energy absorption in

- porous β -type biomedical titanium produced by selective laser melting [J]. *Scripta Materialia*, 2018, 153: 99–103. DOI: <https://doi.org/10.1016/j.scriptamat.2018.05.010>.
- [20] ZHANG L C, ATTAR H. Selective laser melting of titanium alloys and titanium matrix composites for biomedical applications: A review [J]. *Adv Eng Mater*, 2016, 18: 463–475. DOI: <https://doi.org/10.1002/adem.201500419>.
- [21] ZHOU L, CHEN J, LI C, HE J, LI W, YUAN T, LI R. Microstructure tailoring to enhance strength and ductility in pure tantalum processed by selective laser melting [J]. *Mater Sci Eng A*, 2020, 785: 139352. DOI: <https://doi.org/10.1016/j.msea.2020.139352>.
- [22] LIU Y J, WANG H L, LI S J, WANG S G, WANG W J, HOU W T, HAO Y L, YANG R, ZHANG L C. Compressive and fatigue behavior of beta-type titanium porous structures fabricated by electron beam melting [J]. *Acta Mater*, 2017, 126: 58–66. DOI: <https://doi.org/10.1016/j.actamat.2016.12.052>.
- [23] ZHOU L, CHEN J, HUANG W, REN Y, NIU Y, YUAN T. Effects of Ta content on phase transformation in selective laser melting processed Ti-13Nb-13Zr alloy and its correlation with elastic properties [J]. *Vacuum*, 2021, 183: 109798. DOI: <https://doi.org/10.1016/j.vacuum.2020.109798>.
- [24] LI W, YANG Y, LIU J, ZHOU Y, LI M, WEN S, WEI Q, YAN C, SHI Y. Enhanced nanohardness and new insights into texture evolution and phase transformation of TiAl/TiB₂ in-situ metal matrix composites prepared via selective laser melting [J]. *Acta Mater*, 2017, 136: 90–104. DOI: <https://doi.org/10.1016/j.actamat.2017.07.003>.
- [25] LI R, WANG M, LI Z, CAO P, YUAN T, ZHU H. Developing a high-strength Al-Mg-Si-Sc-Zr alloy for selective laser melting: Crack-inhibiting and multiple strengthening mechanisms [J]. *Acta Mater*, 2020, 193: 83–98. DOI: <https://doi.org/10.1016/j.actamat.2020.03.060>.
- [26] NIU P, LI R, ZHU S, WANG M, CHEN C, YUAN T. Hot cracking, crystal orientation and compressive strength of an equimolar CoCrFeMnNi high-entropy alloy printed by selective laser melting [J]. *Opt Laser Technol*, 2020, 127: 106147. DOI: <https://doi.org/10.1016/j.optlastec.2020.106147>.
- [27] ZHOU L, YUAN T, LI R, TANG J, WANG M, MEI F. Anisotropic mechanical behavior of biomedical Ti-13Nb-13Zr alloy manufactured by selective laser melting [J]. *J Alloys Compd*, 2018, 762: 289–300. DOI: <https://doi.org/10.1016/j.jallcom.2018.05.179>.
- [28] ZHOU L, YUAN T, LI R, TANG J, WANG G, GUO K, YUAN J. Densification, microstructure evolution and fatigue behavior of Ti-13Nb-13Zr alloy processed by selective laser melting [J]. *Powder Technol*, 2019, 342: 11–23. DOI: <https://doi.org/10.1016/j.powtec.2018.09.073>.
- [29] ZHOU L, YUAN T, TANG J, LI L, MEI F, LI R. Texture evolution, phase transformation and mechanical properties of selective laser melted Ti-13Nb-13Zr [J]. *Mater Charact*, 2018, 145: 185–195. DOI: <https://doi.org/10.1016/j.matchar.2018.08.053>.
- [30] LIU K, SCHMEDAKE T A, TSU R. A comparative study of colloidal silica spheres: Photonic crystals versus Bragg's law [J]. *Phys Lett A*, 2008, 372: 4517–4520. DOI: <https://doi.org/10.1016/j.physleta.2008.04.008>.
- [31] WEI L S, KIM H Y, MIYAZAKI S. Effects of oxygen concentration and phase stability on nano-domain structure and thermal expansion behavior of Ti-Nb-Zr-Ta-O alloys [J]. *Acta Mater*, 2015, 100: 313–322. DOI: <https://doi.org/10.1016/j.actamat.2015.08.054>.
- [32] ZHONG M, SUN H, LIU W, ZHU X, HE J. Boundary liquation and interface cracking characterization in laser deposition of Inconel 738 on directionally solidified Ni-based superalloy [J]. *Scr Mater*, 2005, 53: 159–164. DOI: <https://doi.org/10.1016/j.scriptamat.2005.03.047>.
- [33] GU D, HAGEDORN Y C, MEINERS W, MENG G, BATISTA R J S, WISSENBACH K, POPRAWE R. Densification behavior, microstructure evolution, and wear performance of selective laser melting processed commercially pure titanium [J]. *Acta Mater*, 2012, 60: 3849–3860. DOI: <https://doi.org/10.1016/j.actamat.2012.04.006>.
- [34] MARI D, KRAWITZ A D, RICHARDSON J W, BENOIT W. Residual stress in WC-Co measured by neutron diffraction [J]. *Mater Sci Eng A*, 1996, 209: 197–205. DOI: [https://doi.org/10.1016/0921-5093\(95\)10147-0](https://doi.org/10.1016/0921-5093(95)10147-0).
- [35] KUO C N, CHUA C K, PENG P C, CHEN Y W, SING S L, HUANG S, SU Y L. Microstructure evolution and mechanical property response via 3D printing parameter development of Al-Sc alloy [J]. *Virtual Phys Prototyp*, 2020, 15: 120–129. DOI: <https://doi.org/10.1080/17452759.2019.1698967>.
- [36] ATTAR H, BÖNISCH M, CALIN M, ZHANG L C, SCUDINO S, ECKERT J. Selective laser melting of in situ titanium-titanium boride composites: Processing, microstructure and mechanical properties [J]. *Acta Mater*, 2014, 76: 13–22. DOI: <https://doi.org/10.1016/j.actamat.2014.05.022>.
- [37] ROBINSON J, STANFORD M, ARJUNAN A. Correlation between selective laser melting parameters, pore defects and tensile properties of 99.9% silver [J]. *Mater Today Commun*, 2020, 25: 101550. DOI: <https://doi.org/10.1016/j.mtcomm.2020.101550>.
- [38] THIJS L, KEMPEN K, KRUTH J P, van HUMBEECK J. Fine-structured aluminium products with controllable texture by selective laser melting of pre-alloyed AlSi10Mg powder [J]. *Acta Mater*, 2013, 61: 1809–1819. DOI: <https://doi.org/10.1016/j.actamat.2012.11.052>.
- [39] ATTAR H, LÖBER L, FUNK A, CALIN M, ZHANG L C, PRASHANTH K G, SCUDINO S, ZHANG Y S, ECKERT J. Mechanical behavior of porous commercially pure Ti and Ti-TiB composite materials manufactured by selective laser melting [J]. *Mater Sci Eng A*, 2015, 625: 350–356. DOI: <https://doi.org/10.1016/j.msea.2014.12.036>.
- [40] AL-BERMANI S S, BLACKMORE M L, ZHANG W, TODD I. The origin of microstructural diversity, texture, and mechanical properties in electron beam melted Ti-6Al-4V, Metall [J]. *Mater Trans A Phys Metall Mater Sci*, 2010, 41: 3422–3434. DOI: <https://doi.org/10.1007/s11661-010-0397-x>.
- [41] HERZOG D, SEYDA V, WYCISK E, EMMELMANN C. Additive manufacturing of metals [J]. *Acta Mater*, 2016, 117: 371–392. DOI: <https://doi.org/10.1016/j.actamat.2016.07.019>.
- [42] YAN Z, LIU W, TANG Z, LIU X, ZHANG N, LI M, ZHANG H. Review on thermal analysis in laser-based additive manufacturing [J]. *Opt Laser Technol*, 2018, 106: 427–441.

- DOI: <https://doi.org/10.1016/j.optlastec.2018.04.034>.
- [43] GAO X, LIN X, YU J, LI Y, HU Y, FAN W, SHI S, HUANG W. Selective laser melting (SLM) of in-situ beta phase reinforced Ti/Zr-based bulk metallic glass matrix composite [J]. *Scr Mater.*, 2019, 171: 21–25. DOI: <https://doi.org/10.1016/j.scriptamat.2019.06.007>.
- [44] LU Y, HUANG Y, WU J, LU X, QIN Z, DAISENBERGER D, CHIU Y L. Graded structure of laser direct manufacturing bulk metallic glass [J]. *Intermetallics*, 2018, 103: 67–71. DOI: <https://doi.org/10.1016/j.intermet.2018.10.005>.
- [45] ZHANG Q, CHEN J, WANG L, TAN H, LIN X, HUANG W. Solidification microstructure of laser additive manufactured Ti-6Al-2Zr-2Sn-3Mo-1.5Cr-2Nb titanium alloy [J]. *J Mater Sci Technol.*, 2016, 32: 381–386. DOI: <https://doi.org/10.1016/j.jmst.2015.11.019>.
- [46] REN Y M, LIN X, FU X, TAN H, CHEN J, HUANG W D. Microstructure and deformation behavior of Ti-6Al-4V alloy by high-power laser solid forming [J]. *Acta Mater.*, 2017, 132: 82–95. DOI: <https://doi.org/10.1016/j.actamat.2017.04.026>.
- [47] QUAN J, LIN K, GU D. Selective laser melting of silver submicron powder modified 316L stainless steel: Influence of silver addition on microstructures and performances [J]. *Powder Technol.*, 2020, 364: 478–483. DOI: <https://doi.org/10.1016/j.powtec.2020.01.082>.
- [48] LI W, LI M, LIU J, YANG Y, WEN S, WEI Q, YAN C, SHI Y. Microstructure control and compressive properties of selective laser melted Ti-43.5Al-6.5Nb-2Cr-0.5B alloy: Influence of reduced graphene oxide (RGO) reinforcement [J]. *Mater Sci Eng A*, 2019, 743: 217–222. DOI: <https://doi.org/10.1016/j.msea.2018.08.087>.
- [49] ZHU Z G, NGUYEN Q B, NG F L, AN X H, LIAO X Z, LIAW P K, NAI S M L, WEI J. Hierarchical microstructure and strengthening mechanisms of a CoCrFeNiMn high entropy alloy additively manufactured by selective laser melting [J]. *Scripta Materialia*, 2018, 154: 20–24. DOI: <https://doi.org/10.1016/j.scriptamat.2018.05.015>.
- [50] WEI K, GAO M, WANG Z, ZENG X. Effect of energy input on formability, microstructure and mechanical properties of selective laser melted AZ91D magnesium alloy [J]. *Mater Sci Eng A*, 2014, 611: 212–222. DOI: <https://doi.org/10.1016/j.msea.2014.05.092>.
- [51] LI C, DING Z, van DER ZWAAG S. The modeling of the flow behavior below and above the two phase region for two newly developed meta-stable β titanium alloy [J]. *Advanced Engineering Materials*, 2020, 1901552: 1–10. DOI: [10.1002/adem.201901552](https://doi.org/10.1002/adem.201901552).
- [52] PARK C H, PARK J W, YEOM J T, CHUN Y S, LEE C S. Enhanced mechanical compatibility of submicrocrystalline Ti-13Nb-13Zr alloy [J]. *Mater Sci Eng A*, 2010, 527: 4914–4919. DOI: <https://doi.org/10.1016/j.msea.2010.04.057>.
- [53] XIAO L, SONG W, HU M, LI P. Compressive properties and micro-structural characteristics of Ti-6Al-4V fabricated by electron beam melting and selective laser melting [J]. *Mater Sci Eng A*, 2019, 764: 138204. DOI: <https://doi.org/10.1016/j.msea.2019.138204>.
- [54] ATTAR H, CALIN M, ZHANG L C, SCUDINO S, ECKERT J. Manufacture by selective laser melting and mechanical behavior of commercially pure titanium [J]. *Mater Sci Eng A*, 2014, 593: 170–177. <https://doi.org/10.1016/j.msea.2013.11.038>.

(Edited by HE Yun-bin)

中文导读

金属钽添加对激光粉床熔化制备钛合金微观组织和力学性能的影响

摘要: 激光粉末床熔化技术(L-PBF)材料库的扩大对材料科学的发展具有重要意义。在本研究中,首次将生物医用钛合金Ti-13Nb-13Zr与不同金属钽(2 wt%~8 wt%)混合后采用L-PBF技术成形。成形合金微观组织由 β 相基体以及部分未熔化的纯钽组成,由于马兰格尼效应的影响,部分未熔化的金属钽沿熔池的边界分布。金属钽熔化吸收了大量的能量,随着金属钽含量的增大,熔池逐渐减小,细小的晶粒分布在熔池的中心。随着重熔现象的出现,在熔池边界处的晶粒增大。由于金属钽引起的晶格不匹配,在未熔化的金属钽附近出现柱状晶转变为等轴晶现象。随着金属钽含量的增加,再结晶组织增强,纤维组织减弱。由于在L-PBF成形过程中细小的马氏体 α' 相析出,样品的压缩强度比传统方法制备的强度高。本研究将为未来采用L-PBF工艺制备生物医学合金提供重要参考。

关键词: 激光粉床熔化; 钛合金; 金属钽; 凝固组织; 组织演变